npj | computational materials

Article

Published in partnership with the Shanghai Institute of Ceramics of the Chinese Academy of Sciences

https://doi.org/10.1038/s41524-026-02044-7

Multiscale kinetic model of ethylene oligomerization in Ni-NU-1000 metal-organic framework

Aleksandr Avdoshin[1], Nikita A. Matsokin[1], Thanh-Nam Huynh[2], Dmitry I. Sharapa[2], Karin Fink[1], Felix Studt[2,3], Wolfgang Wenzel[1] & Mariana Kozlowska[1] ✉

Single-atom catalysts (SACs) provide isolated, well-defined metal sites that are suited for mechanistic modeling in porous materials such as metal-organic frameworks (MOFs). However, the influence of framework topology and mass transport on catalytic outcomes remains poorly understood. Here we develop a multiscale kinetic model for ethylene oligomerization in Ni-grafted NU-1000 that combines density functional theory (DFT)-derived free-energy barriers with adsorption and diffusion descriptors. The framework predicts product distributions under realistic reaction conditions. The simulations show that *flow*-mode operation favors selective C_4H_8 formation across a temperature range. This selectivity window progressively narrows with increasing effective diffusion length and catalytic-site density, as longer residence times enhance chain growth beyond dimerization. In contrast, *batch*-mode operation shifts the product distribution toward heavier olefins. These trends provide practical guidance for tuning operating conditions and material properties to achieve desired selective Ni-MOF catalysts.

Computational catalysis in porous materials such as MOFs and zeolites provides mechanistic insight and quantitative predictions that are essential for interpreting and controlling catalytic performance[1,2]. Depending on the problem, such simulations operate across different length and time scales and are highly effective in identifying reaction trends, mechanistic pathways, and structure-activity relationships[3,4]. However, most computational approaches still treat these components in isolation, which limits their ability to predict the catalytic behavior under realistic reaction conditions. For example, most computational investigations of MOFs and zeolites often focus on either the local chemistry of the catalytic center or the macroscopic transport behavior of the material. They rarely address both components simultaneously[5–8]. Thus, approaches that operate on a single scale are inherently limited[9]: standalone DFT captures active site energetics but cannot describe framework-mediated diffusion or the evolution of product distributions. As a result, the coupling between local reactivity and pore-confined mass transfer remains inaccessible when these methods are used in isolation. Moreover, electronic structure modeling is further challenged by the need to represent both the local coordination environment and the pore confinement while maintaining feasible computational cost. This fact leads to the widespread use of truncated cluster models[5,10,11]. At the same time, the accuracy of DFT is strongly dependent on the functional. Commonly used generalized-gradient approximation (GGA) exchange-correlation functionals were demonstrated to fail in producing reliable reaction energetics[12,13]. In our previous work, we introduced a hierarchical cluster approach that captures both the local coordination environment and the surrounding porous framework, while refining electronic energies using higher-accuracy DFT methods[14]. TPSSh functional was shown to give the best agreement in comparison to the coupled cluster reference.

Since intrinsic reactivity at metal centers is governed primarily by the local electronic environment, whereas catalyst selectivity in porous hosts depends critically on confinement, competitive adsorption, and mass transport, scale-bridging methodologies capable of coupling diverse processes are required. A noticeable illustration of adsorption influence from zeolite simulations aptly highlights this point: the long-invoked "compensation effect" in cracking was attributed to acidity variations, yet later analyses showed that chain-length trends arise predominantly from adsorption strength and the resulting intra-zeolite concentrations[15,16]. Consistent with this view, Bickel and Gounder summarized that dynamic in-pore compositions and diffusional constraints reshape catalytic performance during chain-growth reactions in porous catalysts[17].

An exemplary catalytic reaction in which selectivity, diffusion constraints, and confinement effects strongly influence product distributions is

[1]Institute of Nanotechnology, Karlsruhe Institute of Technology, Karlsruhe, Germany. [2]Institute of Catalysis Research and Technology, Karlsruhe Institute of Technology, Karlsruhe, Germany. [3]Institute for Chemical Technology and Polymer Chemistry, Karlsruhe Institute of Technology, Karlsruhe, Germany. ✉e-mail: mariana.kozlowska@kit.edu

ethylene oligomerization[18]. Its products, for example, linear α-olefins such as but-1-ene, hex-1-ene, and oct-1-ene, are valuable petrochemical intermediates whose industrial relevance depends critically on achieving high selectivity toward specific olefin size[19]. In Ni-based single-atom catalysts used for ethylene oligomerization, the product distribution is governed by a delicate balance between chain-growth and chain-termination steps, making the reaction particularly sensitive to adsorptive and transport phenomena within porous hosts. MOFs therefore provide an attractive platform for tuning this balance, as their well-defined coordination environments and pore architectures allow systematic control over both the intrinsic reactivity of the metal center and the mobility of growing oligomers.

Among the available systems, NU-1000 is especially interesting due to its hierarchical pore architecture: mesochannels enabling efficient mass transport and c-pores hosting well-isolated catalytic centers. Such molecular architecture creates conditions under which both local reaction energetics and pore-level diffusion phenomena influence catalytic behavior[20]. Experimental work of Goetjen et al. suggested that Cr(III)-NU-1000 exhibits measurable catalytic activity under mild conditions with Schulz-Flory selectivity toward C_8−C_{18} products[21], while Li et al. reported that Ni-grafted NU-1000 results in C_4–C_8 oligomers in *flow* mode at 318 K and 2 bar[22]. The latter also undergoes diffusion-driven deactivation via polymer accumulation[22], impacting overall catalytic performance by reducing accessible pore volume and lowering ethylene conversion over time. Structural evidence for active-site localization in the c-pores[23] and DFT screening identifying Ni(II) as a promising center[24] further highlighted NU-1000 MOF as a system where catalytic performance is governed jointly by catalytic active-site chemistry and pore-scale transport. Such behavior of the catalytic system clearly indicates the complex interplay of diverse processes and the necessity of multiscale modeling approaches designed to capture reaction selectivity.

Multiscale kinetic modeling provides a powerful route for linking molecular reaction energetics with macroscopic selectivity. Approaches that combine DFT-derived energy barriers with kinetic approaches, such as kinetic Monte Carlo (kMC) or master-equation methods, enable the exploration of reaction networks beyond the timescales accessible to direct molecular dynamics (MD) simulations[12,25]. However, kMC simulations often become computationally expensive for systems with strongly coverage-dependent adsorption, low-probability events, or slow mass-transfer steps, and require extensive stochastic sampling to achieve convergence. Master-equation solvers offer a deterministic alternative[26–30].

In this work, we developed a deterministic master-equation-based multiscale kinetic model for porous single-atom catalysts. The method is formulated for Ni single-atom sites in NU-1000 MOF (Ni-NU-1000). It couples corrected DFT Gibbs free energy barriers with adsorption and diffusion interpolation-extrapolation models, as well as a master-equation reactor model of *flow* and *batch* olefin oligomerization reaction. We quantify how realistic reactor operating conditions (300–600 K, 1–50 bar) reorganize termination of product pathways and, together with coverage-dependent co-adsorption and reactor mode (*flow* vs. *batch*), steer the α-olefin distribution beyond what the intrinsic energy profile would suggest. This establishes practical levers, namely, MOF framework topology and catalytic site density, combined with reactor configuration, to provide a transferable computational workflow for other MOF-based catalytic systems. Ultimately, this multiscale framework enables us to connect local reaction energetics with framework-mediated adsorption and diffusion, providing quantitative insight into how operating conditions and material parameters shape the olefin product distribution.

Results

Kinetic model

To quantify how chemical reactions together with mass transfer during ethylene oligomerization influence the evolving product distribution, we constructed a multiscale framework that links reaction energetics, obtained from electronic structure calculations, with adsorption and diffusion of molecular species in NU-1000 MOF calculated using all-atom Grand canonical Monte Carlo (GCMC) and transition-state theory (TST)-based diffusion analysis (see Fig. S1–S5). The DFT-based reaction energetics, GCMC-derived adsorption capacities, and transition state theory (TST)-based diffusion coefficients were combined via a master equation whose boundary conditions were modified to emulate experimental *flow* and *batch* operating modes through controlled exchange of species with an external reservoir rather than explicit reactor hydrodynamics. The schematic visualization of the computational workflow is depicted in Fig. 1. The Gibbs free energy profile (see Fig. 1b), obtained from DFT calculations and corrected within the hierarchical cluster approach[14], provided the $\Delta G^{\ddagger}$ values for all elementary reactions. They were applied for the calculation of the corresponding reaction rates using the Eyring equation (see panel E in Fig. 1). All-atom force-field–based GCMC/MC simulations of co-adsorption were used to determine the in-pore and reservoir phase loadings (and thus the thermodynamic driving forces for molecular exchange), while Widom-insertion free-energy profiles combined with transition-state theory (TST) were used to estimate diffusion coefficients. The corresponding adsorption isotherms and diffusion coefficients used in the model are summarized in panels A and C of Fig. 1, respectively.

The system was formulated as two coupled phases: the NU-1000 framework, where oligomerization occurs, and a reservoir gas phase in which no reaction takes place. Based on the chemical-potential differences between these phases, we evaluated the diffusive flux of olefins entering and leaving the MOF. All simulations were performed under isothermal conditions, with the temperature treated as a fixed external parameter and assumed to be uniform across both the MOF framework and the gas-phase reservoir. The magnitude and reversibility of this exchange were set according to the reactor scenarios represented in Fig. 1d, with computational details provided in the "Methods" section.

All the rates defined a coupled set of differential equations representing both chemical reactions together with non-reactive mass-transfer steps (examples of these differential equations and catalytic reaction network are provided in Supplementary Information (Tables S1–S6) and Eq. (4)). By modifying the boundary conditions, the model is capable of simulating various reactor scenarios. In the *flow* configuration, ethylene is supplied at constant concentration while heavier olefins (from C_4H_8 and beyond) are removed irreversibly from the reservoir gas phase, mimicking continuous operation. In contrast, the *batch* mode allows reversible exchange between the MOF and reservoir gas phase (details provided in the Methods section).

In accordance with Fickian diffusion, the characteristic mass-transfer rate scales as $k \propto D/L^2$. The effective mass transfer depends not only on the self-diffusion coefficient D but also on the diffusion length L; thus, our model included the effective diffusion length, which defines the average diffusion path that olefins must traverse during the reaction. Values of L were selected based on experimentally reported NU-1000 crystallite dimensions, ranging from 300 nm to 10 μm, which correspond to diffusion within individual particles[31]. In these cases, transport is modeled assuming diffusion inside an isolated spherical crystallite characterized by the chosen L. To account for transport across interconnected particles under *flow* conditions, larger effective diffusion lengths of 100 μm and 1000 μm were additionally considered. These effective diffusion lengths enter directly into the diffusion term of the kinetic model as the characteristic transport distance controlling the mass-transfer rate constant, without implying a one-to-one correspondence with the size of a single MOF particle. Finally, we included an *infinite-crystal* mode, equivalent to a pure DFT description in which no reservoir gas phase is present, and mass transfer out of the MOF is absent. Details of each part of our model are discussed in "Methods".

Reaction mechanism and energy profile

Free energies presented herein were computed using a hierarchical cluster approach proposed in our previous work[14], in which the energy was computed at the PBE-D3(BJ) level using a periodic model and subsequently corrected to the TPSSh-D3(BJ) level using a small cluster model (see Fig. 2a and "Methods" section). The obtained free energy profile, shown

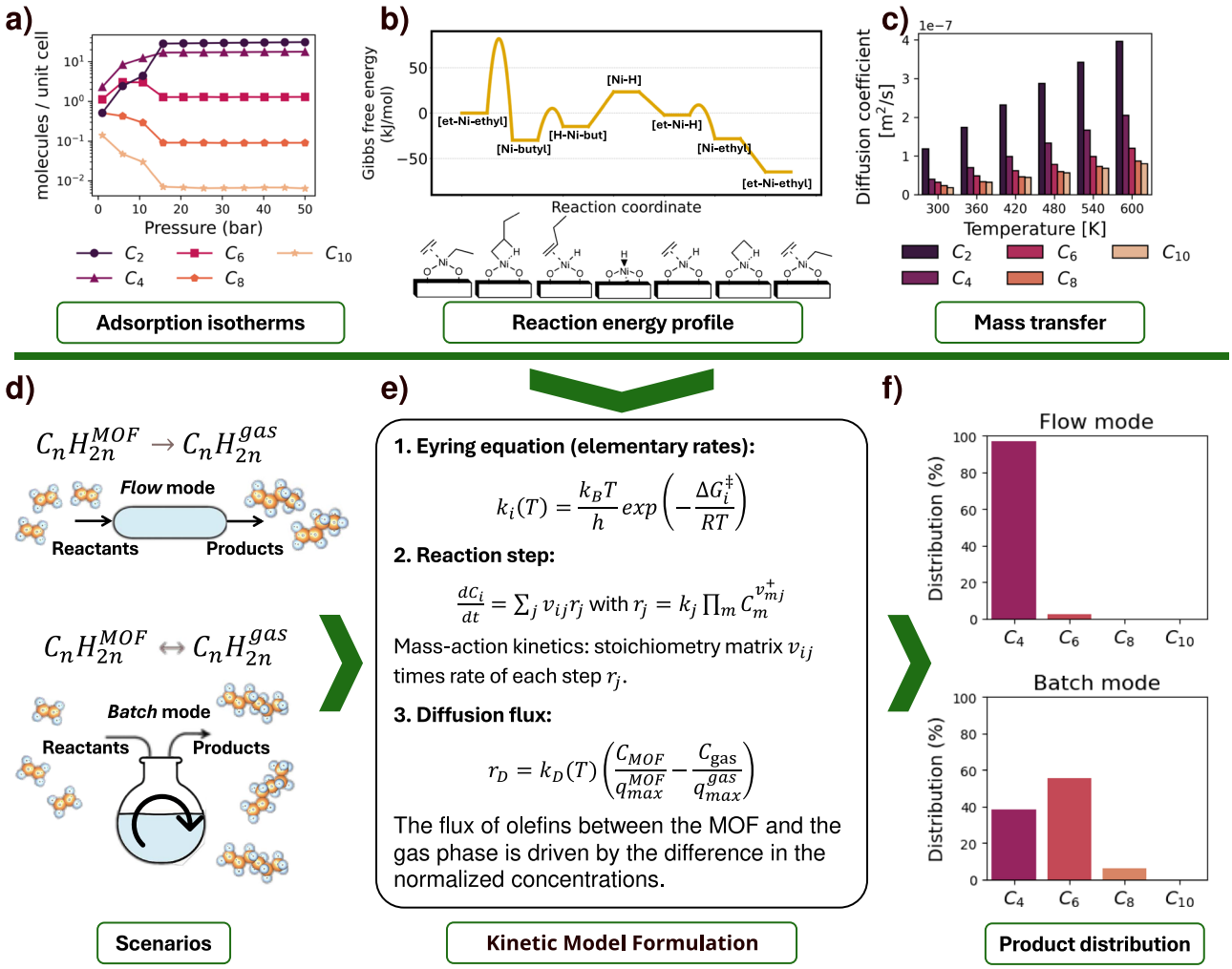

Fig. 1 | Multiscale kinetic-model workflow for ethylene oligomerization in Ni-grafted NU-1000. The workflow combines: **a** adsorption properties of α-olefins in the MOF (e.g., adsorption and co-adsorption isotherms)[7]; **b** DFT reaction energy profiles[14]; **c** mass-transfer (diffusion coefficients); **d** reactor conditions; **e** a kinetic model based on Eyring theory, mass-action master equations, and diffusion steered by MOF porous architecture and reservoir gas phase chemical potentials; **f** a condition-dependent product distribution.

schematically in Fig. 1b and in full in Fig. S6, corresponds to the oligomerization of ethylene *via* a linear insertion Cossee-Arlman type mechanism over square planar Ni(II) active sites in the NU-1000 framework. This reaction mechanism and the nature of the catalyst were elucidated in detail in our previous work[14], in agreement with the literature[5,6,10,24,32,33].

Reaction initiation begins with (I) ethylene adsorption on the Ni site, forming a π-complex, followed by (II) formation of the first Ni–alkyl species via coupling of the coordinated ethylene to the Ni site. A second ethylene molecule subsequently coordinates to the Ni–alkyl intermediate (III). Migratory insertion of ethylene into the Ni–C bond then produces a longer Ni–alkyl species (IV), completing one propagation step of the Cossee–Arlman mechanism.

From this point, two competing pathways are possible. Propagation proceeds via repeated ethylene coordination and migratory insertion (Steps III–IV), leading to continued chain growth and the formation of higher α-olefins. Alternatively, chain stopping occurs via β-hydride elimination from the Ni–alkyl intermediate, generating a Ni–H species with a coordinated α-olefin (VI). Following β-hydride elimination, two distinct pathways are accessible. In the first, the coordinated olefin desorbs directly from the Ni site, releasing the product and regenerating the catalytically active site (VII). In the second, ethylene coordinates to the post-elimination Ni–H/olefin complex (VIII), promoting displacement of the coordinated olefin and enabling re-entry into the propagation manifold. Subsequent desorption of the coordinated α-olefin completes product release and restores an ethylene-bound or vacant active site (IX) (see Fig. 2b)

The reaction energy profile in Fig. S6 shows that both termination routes are thermodynamically possible, but differ in activation energy. The balance between these pathways depends on temperature and olefin pressure. The full catalytic reaction network, shown in Fig. 2b, is mechanistically detailed but leads to numerical instabilities when combined with the Eyring-rate formalism. This arises because the network contains barrierless and near-barrierless elementary steps, for which transition-state theory is formally ill-defined and yields unphysically large rate constants. To ensure numerical stability and a physically meaningful kinetic model, such steps were either merged into composite reactions or absorbed into adjacent elementary steps with an effective activation barrier. For the purpose of kinetic modeling, the network was therefore reduced to two dominant reaction classes, as illustrated in Fig. 2c. These comprise (i) chain growth via migratory insertion of C_2H_4 and its reverse (reverse migratory insertion), with rate constants r_{ins} and $r_{reverse}$ — ins, and (ii) chain termination and its reverse (de-termination), with rate constants r_{ter} and r_{deter}. Based on the energy profile, this reduced description is valid over the majority of the investigated pressure–temperature space. Only at the highest temperatures combined with low pressures does the assumed π-complex [ethyl–Ni–ethylene] become thermodynamically unstable, with the bare [Ni–ethylene] species becoming dominant. As this regime lies outside the

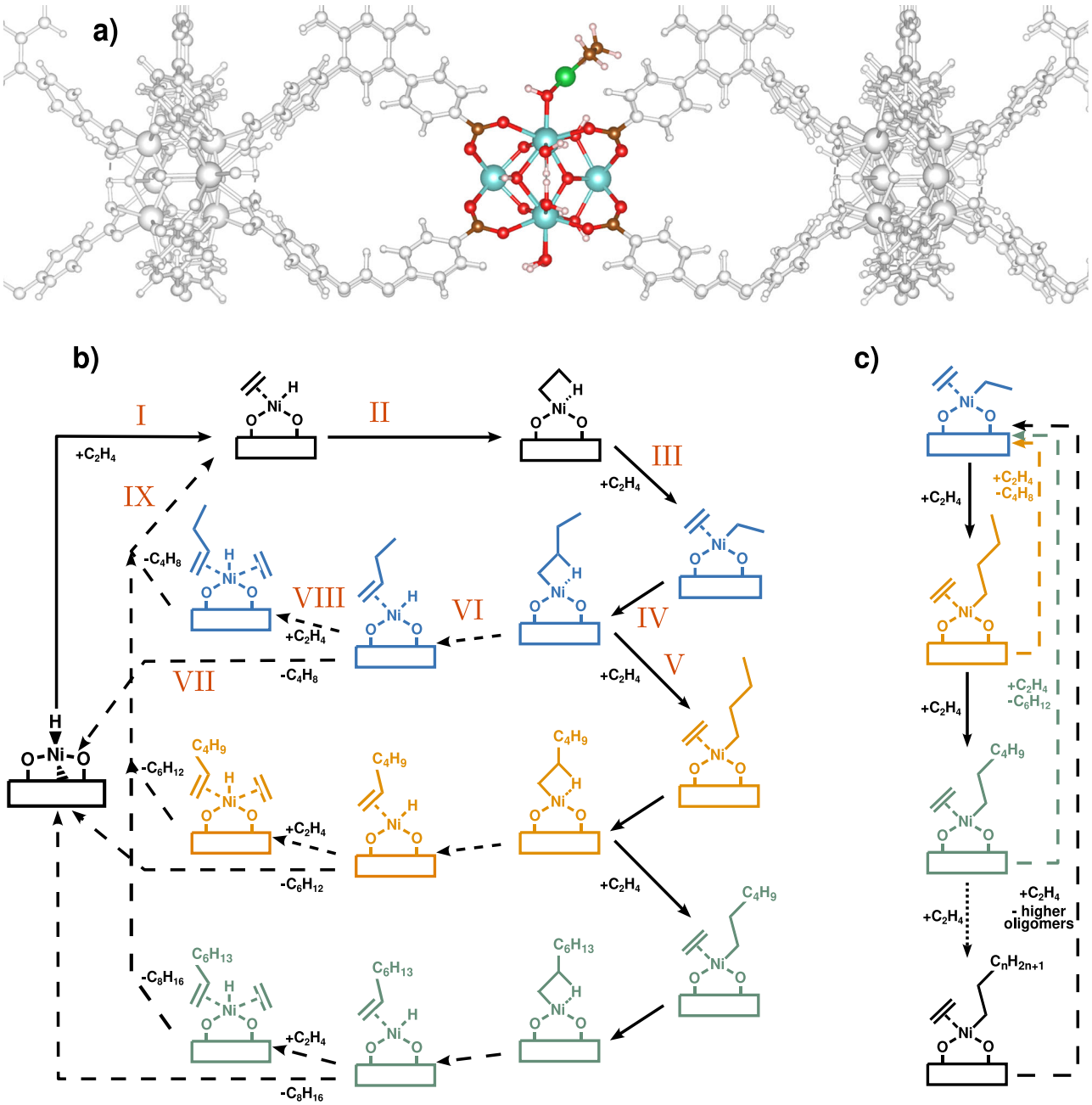

Fig. 2 | Reaction mechanism and energy profile for ethylene oligomerization in Ni–NU-1000. a Schematic illustration of the hierarchical cluster approach, in which the whole periodic structure of the MOF is modeled at the PBE-D3(BJ) level of theory, while the colored region represents the formate cluster used for corrections at the TPSSh-D3(BJ) level. In the visualization, different atoms in the cluster model are represented by specific colors: Zr (cyan), Ni (green), O (red), C (brown), and H (white). **b** Complete and **c** simplified catalytic reaction network of ethylene oligomerization in Ni-NU-1000. The complete scheme is shown up to C_8H_{16} formation and was calculated with DFT. The simplified scheme contains up to 16 carbon atoms in the olefin chain. Parameters for these molecules were obtained by extrapolation of Gibbs free energy barriers. In (**b**) and (**c**), the solid arrows link to chain growth reactions, the dashed arrows link to chain elimination reactions.

experimentally relevant operating conditions for Ni–MOF–based ethylene oligomerization, it was excluded from the kinetic analysis. For the termination channel, the rate-determining barrier was selected as the highest free-energy transition state among the two competing pathways connecting the chain-growth and termination manifolds.

Examples of the reaction rates from the catalytic reactions network in Fig. 2b are provided in Tables S1–S6. The rate-determining barrier varies with pressure and temperature for all simulated stages, from dimerization to tetramerization (see Figs. S7 and S8). In the case of dimerization, several different stages can act as the dominant barrier depending on conditions. By contrast, for higher oligomers such as the tetramer, the rate-determining stage mostly corresponds to the transition state associated with ethylene coordination and Ni-C bond formation.

While the insertion barrier remains nearly constant at 81.4 ± 0.9 kJ mol^{-1}, the reverse-insertion (127.0 ± 9.2 kJ mol^{-1}), termination (64.1 ± 13.8 kJ mol^{-1}), and de-termination (66.6 ± 9.8 kJ mol^{-1}) barriers show substantially larger variations with similar trends: they decrease with increasing temperature and increase with higher pressure. For termination and de-termination, small deviations from this monotonic behavior were observed due to competition between alternative pathways. We note that the Gibbs free energy profile was computed explicitly up to tetramerization and that the rate constants for heavier oligomers were obtained by extrapolation

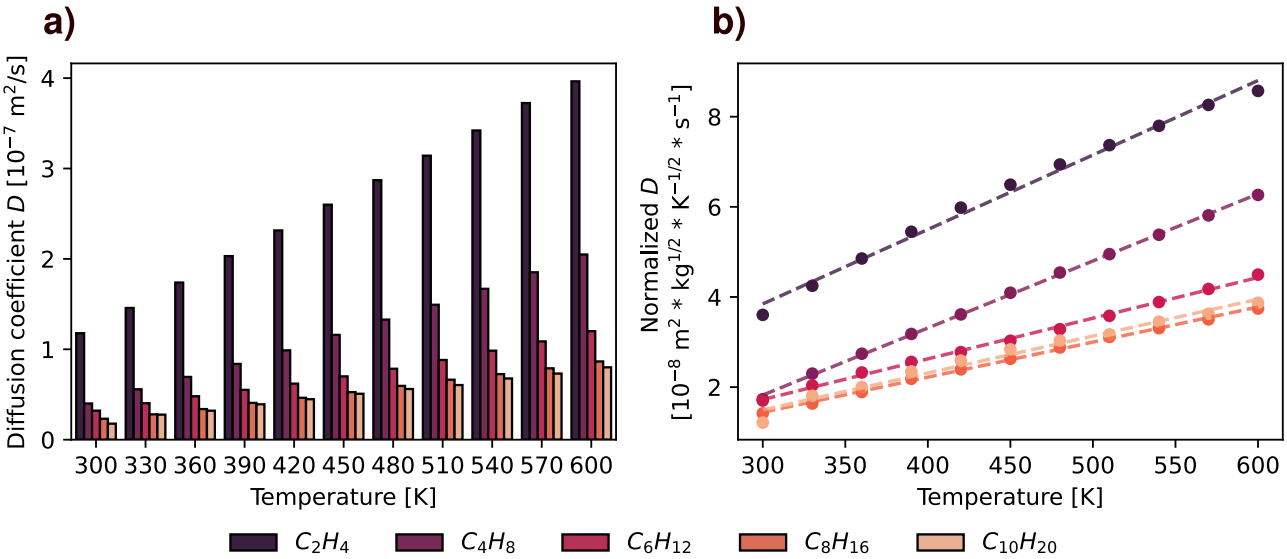

Fig. 3 | Diffusion of olefins in NU-1000 MOF. a Diffusion coefficients of different olefins in NU-1000 MOF as a function of temperature. **b** Normalized diffusion coefficients as a function of temperature.

up to $C_{16}H_{32}$, assuming the same activation barriers as for the tetramerization step.

The rate-ratio constants $K_{growth} = r_{ins}/r_{reverse\text{-}ins}$ and $K_{termination} = r_{ter}/r_{deter}$ exhibit distinct temperature and pressure dependencies (see Fig. S9). K_{growth} decreases with increasing temperature, whereas $K_{termination}$ increases. With respect to pressure, K_{growth} increases monotonically, while $K_{termination}$ remains essentially pressure independent (see Fig. S9).

Adsorption and diffusion of olefins in NU-1000

GCMC simulations were performed to characterize olefin adsorption in NU-1000 across the temperature-pressure range relevant to the kinetic model. All simulations were carried out assuming an ideal-gas reservoir, with only gaseous olefin phases considered and no liquid condensation. The simulations followed the protocol established in our previous work[7], with additional data points included for both single-component C_2H_4 isotherms used to define the initial in-pore ethylene loading and for the co-adsorption of C_2H_4–$C_{10}H_{20}$ mixtures to refine the interpolation-extrapolation scheme (vide infra) employed in this study. The resulting adsorption behavior is fully consistent with our earlier observations: C_2H_4 exhibits a Type-I isotherm indicative of strong host-guest interactions (see Fig. S5a), whereas the mixture isotherms show the expected competitive and non-monotonic loading trends arising from displacement of heavier olefins (C_8H_{16}–$C_{10}H_{20}$) by lighter ones and the intermediate behavior of species such as C_6H_{12} (see Fig. S3). These results reinforce the necessity of treating multi-component co-adsorption explicitly rather than relying on single-component adsorption data.

Co-adsorption behavior of C_2H_4–$C_{10}H_{20}$ olefins was represented using an interpolation-extrapolation model trained on the GCMC data, employing a *k*-nearest neighbors algorithm for C_2H_4–$C_{10}H_{20}$ species, linear regression for heavier chains ($C_{12}H_{24}$–$C_{16}H_{32}$), and a Langmuir fit for single component C_2H_4. This approach provided the continuous (T, p)-dependent adsorption profiles of all species required for the kinetic simulations (see Fig. 1). We modeled MOF–gas exchange using direction-resolved fluxes as discussed in "Methods" section. Although relative adsorption strengths between different species can vary by several orders of magnitude across pressure-temperature conditions, adsorption is therefore treated as one of the relevant contributions in the kinetic model. A detailed description of the interpolation model and full adsorption analysis is explained in Methods and in our previous publication[7].

The diffusion coefficients used in this work are obtained from test-particle (Widom) insertion simulations at infinite dilution, corresponding to single-component self-diffusivities in the MOF and neglecting olefin–olefin interactions. As shown previously for NU-1000[34], increasing hydrocarbon loading leads to a non-monotonic change in self-diffusion coefficients, with an initial increase followed by a decrease at higher loadings; however, the overall variation remains within less than one order of magnitude. We therefore expect the infinite-dilution diffusivities to slightly underestimate effective diffusivities under reaction conditions. However, in the reactor-scale simulations, transport limitations are governed by the characteristic flux scaling $J \propto D/L^2$ (see "Methods" section), where the effective diffusion length L spans several orders of magnitude, rendering moderate loading-induced variations in D secondary for the predicted kinetic and selectivity trends. Accordingly, free-energy profiles from Widom insertion simulations were analyzed using TST to characterize the diffusion barriers. Although the barriers (see Fig. S2) show some anisotropy across the crystallographic axes, the overall trends are consistent: diffusion slows markedly with increasing olefin size and accelerates with temperature due to the thermal softening of the Gibbs free-energy barriers (see Fig. 3a). The resulting diffusion trends agree well with our previous MD-mean square displacement analysis of olefin transport in NU-1000[7], which likewise revealed anisotropic pathways and a systematic decrease in mobility with increasing oligomer length. The absolute diffusion coefficients obtained from the TST analysis are systematically higher than those extracted from MD simulations, with a maximal overestimation of approximately a factor of seven. This deviation depends on the adsorbate loading, and thus indirectly on pressure, but remains within the same order of magnitude. This is expected for transition-state-based estimates because TST neglects dynamical recrossing of the free-energy barrier and therefore systematically overestimates the rate of successful hops. Despite this quantitative offset, both approaches yield fully consistent qualitative trends in chain-length and temperature dependencies.

To use these data within the reactor model in Fig. 1c, we converted the direction-resolved diffusivity into a temperature-dependent interpolation model that enables continuous evaluation of diffusivity inside NU-1000 during the kinetics. Normalization of the diffusivities for removing the molecular weight and prefactor contributions revealed two distinct transport regimes. Light olefins (C_2H_4–C_4H_8) exhibited a strong temperature response, whereas heavier species (C_6H_{12}–$C_{10}H_{20}$) fall into a confinement-dominated regime with much weaker thermal sensitivity (see Fig. 3b). We used this crossover to extrapolate diffusion coefficients for olefin oligomers beyond C_{10} and to construct a smooth chain-length-dependent diffusion

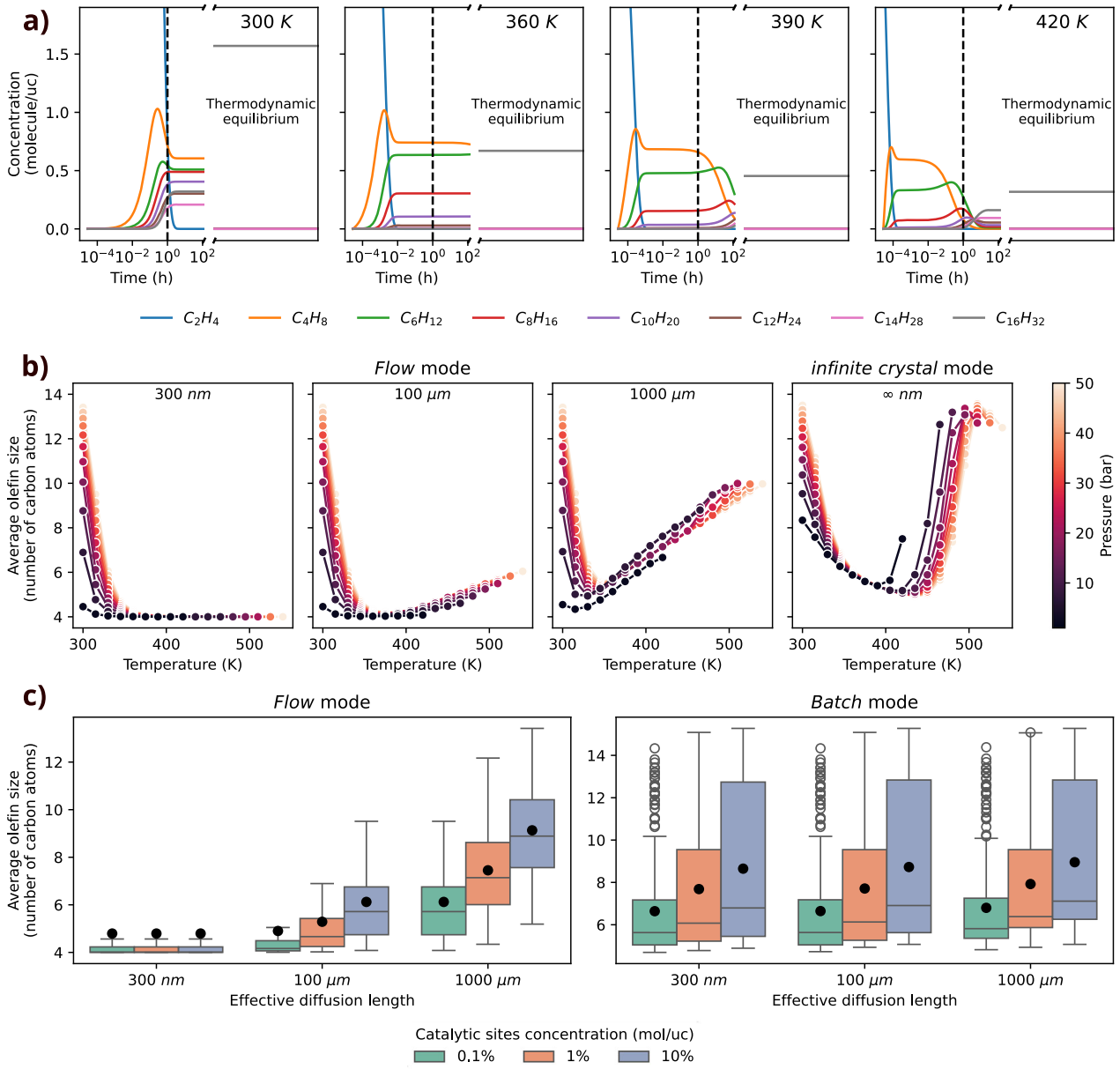

Fig. 4 | Olefin product distribution under different conditions. a Time evolution of olefin concentrations at various temperatures in the *infinite-crystal* model. The dashed vertical line indicates the reference time of 1 h used for comparative analysis. The continuous time axis displays kinetic evolution up to 100 h, while the broken axis extends to the thermodynamic limit, where the equilibrium composition is obtained from the Boltzmann distribution. **b** Average number of carbon atoms in the produced olefin as a function of temperature and pressure for the *flow* mode at effective diffusion length of 300 nm and 100 μm and 1000 μm (first three panels from the left), compared with the *infinite-crystal* model that neglects diffusion and MOF adsorption capacity effects (on the right). Each point represents the data collected after 1 h simulated time. **c** Average olefin size as a function of the catalytic-site concentration for the *flow* and *batch* modes and different effective diffusion lengths. Olefin distributions were evaluated at a fixed simulation time of 1h across the full range of simulated pressures (1–50 bar) and temperatures (300–600 K), using the filtered dataset. Each box represents the interquartile range, with the horizontal line indicating the median. Whiskers extend to 1.5 times the interquartile range; values outside this range are shown as white circles with black edges, and black dots denote the mean.

dataset for integration into the kinetic framework. Full methodological details are provided in "Methods" section.

Kinetic model for ethylene oligomerization in Ni-NU-1000

As presented above, the multiscale kinetic model developed in this work was applied to simulate *flow* and *batch* mode experimental conditions. They were applied considering the effective diffusion length of 300 nm, 100 μm and 1000 μm. Here, we present how the change in these conditions impacts the distribution of the products formed during ethylene oligomerization reaction. However, the steady-state behavior is first explained to clarify its role in shaping the overall reaction dynamics.

In kinetic simulations of the *infinite-crystal* model (see Fig. 4a), which track the time evolution of reactant and product concentrations, the reaction sequence begins with the rapid formation of but-1-ene, followed by the growth to hex-1-ene and heavier oligomers. At 300 K, this progression produces pronounced transient peaks in the concentrations of C_4H_8 and C_6H_{12}. At higher temperatures (360–420 K), only C_4H_8 exhibits a noticeable transient peak, whereas C_6H_{12} and heavier species do not show peaks. This reflects the much faster growing and decomposition kinetics at elevated temperatures: heavier oligomers (than C_4H_8) do not persist long enough to form a detectable peak for C_6H_{12} before being driven back toward monomers. Thus, the presence or absence of such transient peaks is a

characteristic signature of the balance between forward oligomerization and backward cracking reactions, providing a kinetic fingerprint of the temperature-dependent stability of each intermediate.

After the peaks, a transient steady state is observed, and the time required to reach this regime decreases with increasing temperature, occurring approximately at 5×10^{0}, 1×10^{-2}, 5×10^{-3}, and 5×10^{-4} h for 300, 360, 390, and 420 K, respectively. This behavior correlates with the depletion of C_2H_4 in the system. In the pseudo-steady state, C_4H_8 dominates across all temperatures; however, the presence of heavier olefins varies significantly. At 300K, oligomers from C_4H_8 up to $C_{16}H_{32}$ are present. As the temperature increases to 360K, the distribution narrows to species up to $C_{10}H_{20}$. This trend continues, and by 420K the system contains only C_4H_8–C_8H_{16}, reflecting the decreasing stability of heavier oligomers at elevated temperature (see Fig. 4a).

Although ethylene regeneration is thermodynamically accessible, its kinetics are significantly slower than those of the forward insertion steps (see Table S1). Consequently, light olefins decompose back to monomers only on very long timescales. Increasing temperature markedly accelerates this decomposition pathway (see Table S2). As a result, at 390 K and 420 K, a clear shift in the product distribution toward heavier olefins is observed, indicating a transition from a kinetically controlled pseudo–steady state toward a thermodynamic steady state. In this regime, the most stable long-chain species, such as $C_{16}H_{32}$, dominate the product distribution across the examined temperature range (see Fig. 4a). We note that the reaction network implemented in the model considered the formation of olefins up to $C_{16}H_{32}$. Consequently, if the kinetic model reaches a state in which $C_{16}H_{32}$ becomes the dominant or exclusive product, this fact should be interpreted as a preference for forming even longer polymeric chains, with the actual product distribution lying beyond the upper limit of our model.

To analyze the olefin distribution under different conditions, we report the composition at a fixed simulation time of 1 h, which serves as a consistent comparison point across all kinetic runs. The distribution at this time is characterized by the average olefin size, defined as

$$\langle L \rangle = \sum_i p_i N_i, \tag{1}$$

where N_i is the number of carbon atoms in the olefin C_nH_{2n} and p_i is its normalized molar fraction.

In the *flow* mode, where a constant inflow of C_2H_4 is maintained (see three panels from the left in Fig. 4b), the average olefin size decreases with increasing temperature from 300 K to 330 K. The magnitude of this decrease depends on pressure: from 4.5 to 4 at 1 bar and from 13.8 to 4 at 50 bar. This initial decrease in average olefin size correlates with an increase in the termination ratio $K_{\text{termination}} = r_{\text{ter}}/r_{\text{deter}}$ (see Fig. S9), indicating an increase of chain termination over re-entry into the growth cycle. Above 330 K, the product distribution becomes increasingly dependent on the effective diffusion length: for 300 nm, C_4H_8 remains the primary product, whereas for larger diffusion lengths, the distribution shifts toward heavier olefins with increasing temperature. At higher pressures and larger effective diffusion lengths, the shift toward heavier olefins becomes more pronounced. A longer residence time of olefins within the MOF increases the probability of re-adsorption and further chain growth, whereas olefins that diffuse out of the MOF effectively exit the catalytic cycle and cannot re-enter. This phenomenon is referred to throughout this paper as *diffusion-controlled termination* in the present kinetic context. If olefins remain sufficiently long within the catalytic cycle, they tend to form long-chain olefins, which align with the experimental observations of Li et al.[22], who reported catalyst deactivation within the first 10 h on flow, attributed to the accumulation of long-chain- and polymeric products.

For the *infinite-crystal* and *batch* modes, the results are qualitatively similar; therefore, we depict the product formation for the former in Figs. 4b and S10. In both cases, the calculated product type exhibits a non-monotonic temperature dependence, featuring the decrease in heavier oligomers formation from 300 to intermediate temperatures (400–450 K, depending on pressure) and a subsequent increase in heavier olefin products at 450–520 K. The initial decrease in average olefin size corresponds to the behavior observed in the flow mode and is similarly associated with an increase in $K_{\text{termination}}$. However, in the *infinite-crystal* model there is no *diffusion-controlled termination* because products cannot leave the framework. Instead, the reaction is simply truncated at 1 h of simulated time, before the desorbed α-olefins have sufficient time to re-adsorb and continue growing. As a result, the decrease is noticeably weaker than in the flow mode, where irreversible removal by diffusion dominates the termination process.

The subsequent growth can be interpreted kinetically as a consequence of the enhanced reverse-insertion rate, which increases from $10^{-11}s^{-1}$ at 300 K to $10^{-3}s^{-1}$ at 420 K, and the accelerated formation of monomeric C_2H_4 (see Fig. S9). This interpretation is supported by simulations without reverse insertion mechanism, represented in Fig. S13, where a slow decrease of product mass is observed without the second increase. Taken together, these results show that in *flow* mode, the oligomerization landscape is governed by the interplay of intrinsic reaction kinetics with *diffusion-controlled termination*, whereas each reactor mode imposes a distinct balance between chain-propagation and chain-ending processes.

We also estimated the turnover frequency (TOF) for the *flow*-mode simulations (see Fig. S14a), defined as the rate of ethylene consumption per active site. The calculated TOFs increase exponentially with temperature and exhibit a sublinear power-law dependence on pressure, as shown by the nearly straight trends on a log–log scale (see Fig. S15). Across the full range of conditions, TOF values span from 3.5×10^{3}–1.9×10^{4} h^{-1} at 300 K to about 2×10^{10} h^{-1} at 540 K. To quantify proximity to steady state, we define a steady-state metric, S, as the ratio of the second to the first derivative of ethylene conversion with respect to time. The smaller S is, the closer is the steady state, see Fig. S14b: S increases with temperature from ~10^{-14} to ~10^{-8} h^{-1} for particles with an effective diffusion length of 300 nm, while for larger particles it reaches values up to ~10^{-2} h^{-1}. The stronger temperature dependence observed for larger particles indicates a progressively larger deviation from steady-state behavior under these conditions.

These simulated trends are consistent with experimental observations that nickel-MOF catalysts can exhibit high intrinsic activities in ethylene oligomerization. For example, Song et al. reported that a diimine-Ni@PCN-701 system reached a TOF of 43,800 h^{-1} at 20 °C and 20 bar in the presence of Et_2AlCl co-catalyst[35], while Chen et al. observed an even higher TOF of 352,000 h^{-1} for Ni-MOF-5 at 35 °C and 50 bar[36]. Although co-catalysts substantially enhance TOF in these experimental systems, the present kinetic model assumes that all catalytic sites included are fully accessible and equally active throughout the reaction and does not account for catalyst deactivation, which can lead to TOF reduction in real systems.

The calculations described above were performed assuming that 1% of the NU-1000 unit cells contain a Ni-based catalytic site. Although typical experimental loadings range from 1 to 5%[37–39], we systematically examined scenarios in which 0.1%, 1%, and 10% of the unit cells host an active Ni site. Across all simulations, we observed that variation in the catalytic-site concentration shifts the product distributions while preserving their overall shape (see Fig. S11 and S12). For both *flow* and *batch* modes, a consistent trend is observed: increasing the number of active sites leads to longer olefin chains (see Fig. 4c). However, in the *flow* mode this effect is substantially more pronounced: both the interquartile range and the median olefin size increase with the catalytic-site density, and the magnitude of this shift depends strongly on the effective diffusion length because of the *diffusion-controlled termination*. In contrast, in the *batch* mode, the interquartile range and median remain nearly unchanged across different diffusion lengths, with the mean olefin size stabilizing around 7–9 carbons regardless of effective diffusion length. This demonstrates a clear trend of increasing olefin size with higher catalytic-site concentrations under the simulated reaction conditions, due to the enhanced probability of olefin interaction with the Ni catalytic site, which promotes further chain growth.

Discussion

In this work, we presented a multiscale kinetic model that couples DFT-derived Gibbs free-energy barriers with adsorption and diffusion descriptors

in the master-equation model of Ni-catalyzed ethylene oligomerization in NU-1000 MOF. This approach allowed us to disentangle how elementary-step reaction energetics, co-adsorption, and mass transport collectively determined oligomerized product distribution under experimentally relevant reactor operating conditions. To assess the role of mass transfer, we compared the kinetic simulations of *infinite-crystal* model with *batch* and *flow* modes that include adsorption capacity and diffusion. To highlight the necessity of a kinetic treatment, we also examined steady-state Boltzmann distributions, which predict the formation of long-chain olefins, consistent with the transport-limited deactivation due to polymer accumulation observed experimentally[22].

The simulations revealed that diffusion, driven by chemical-potential differences between olefins inside NU-1000 and in the external reservoir, plays a critical role in selectivity. With increasing temperature, the formation of C_4H_8 accelerated, enhancing ethylene conversion with selectivity towards C_4H_8. However, the subsequent formation of long-chain olefins also became faster, which increased the risk of long-chain olefin growth, pore blocking, and catalyst deactivation. This behavior defined a preferred temperature window for selectively producing short olefins. The window narrowed substantially with increasing effective diffusion length: while small particles (300 nm) showed optimal selectivity in the 350–600 K range, at 100 μm the window narrowed to 350–420 K, and at 1000 μm the temperature window became very small at 330 K with noticeable presence of heavier olefins (C_6H_{12}–C_8H_{16}). The effective *infinite-crystal* limit restricted this to higher temperatures with even greater presence of (C_6H_{12}–C_8H_{16}) olefins. (see Fig. 4b).

The calculations showed that pressure further modulates the product distribution. At low pressures, lighter olefins were favored, particularly below 350 K, effectively widening the temperature window under *flow* mode conditions. In contrast, in *batch* mode and in the *infinite-crystal* model, decreasing pressure narrowed the window even further, since slower desorption and weaker mass transfer promoted chain growth. These comparisons underscored that only kinetic simulations incorporating realistic mass-transfer effects, rather than the DFT Gibbs free energy profile or thermodynamic models alone, can reliably capture the selectivity trends observed under practical reaction conditions.

Another key factor influencing selectivity, beyond mass transfer and its pressure-dependent and temperature-dependent diffusion rates and phase capacities, is the variation of the intrinsic reaction barriers and rates with operating conditions. While the elementary rates scale with temperature through the Eyring equation prefactor and exponential activation term, the underlying free-energy barriers themselves are not constant. In our system, all barriers, except insertion, showed systematic shifts with thermodynamic conditions: they decreased with temperature elevation and increased with pressure growth. Consequently, pressure affected the chemical rate constants only indirectly, through its influence on the activation barriers. As a result, the ratio constant for chain growth, K_{growth}, decreased with rising temperature and decreasing pressure, indicating a shift toward shorter olefins under these conditions. In contrast, the termination ratio $K_{termination}$ showed another trend: it increased with temperature and did not depend on pressure. With increasing the density of catalytic sites, the product distribution systematically shifted toward heavier olefins, especially under flow-mode operation. It happened because faster local consumption of ethylene increased the probability of chain growth before desorption. This shift varies strongly with the effective diffusion length in the *flow* mode, where mass-transfer limitations significantly reshape the product distribution, whereas in the *batch* mode, the corresponding changes remain nearly identical across all diffusion lengths.

Since the experimental reports for the ethylene oligomerization in Ni-NU-1000 MOF are limited, we compared the results obtained using our model to other porous MOF catalysts known in the literature. Our trends are in good agreement with the experimental study of Yeh et al.[40], who investigated Ni/UiO-66 under *flow*-mode conditions (443-503 K, 1–18 bar) without a co-catalyst. UiO-66 shares the same Zr_6 metal-oxo nodes as NU-1000, making it a closely related comparison system. Yeh et al. reported nearly exclusive C_4H_8 formation, which aligns with our predictions for *flow*-mode operation at short effective diffusion lengths (see Fig. 4b). They also measured a rate that increased linearly with pressure and exponentially with temperature, consistent with the TOF sublinear pressure dependence and strong Arrhenius-type temperature response obtained from our kinetic simulations (see Figs. S14–S15). These trends are further consistent with experimentally reported temperature regimes for Ni-supported MOF-based oligomerization catalysts[5,19,41]. In contrast, Ni-AIM-NU-1000 was reported to produce a broad oligomer distribution containing significant amounts of C_4H_8, C_6H_{12}, and C_8H_{16}[41], together with substantial polyethylene formation under continuous-flow conditions. Liu et al. demonstrated that post-synthetic modification of the node environment with Facac/Acac ligands, which enforced more isolated and well-defined Ni sites with altering reaction energy profile, narrowed this broad distribution to nearly exclusive C_4H_8 formation. Such an observation is again in good qualitative agreement with the trends obtained from our kinetic model (see Fig. 4b, c). Although in experiments the MOFs differ in topology and linker environment from Ni-NU-1000, the systems share a common mechanistic feature: isolated Ni sites that predominantly promote the Cossee-Arlman insertion pathway. This explains why they exhibit strong dimer selectivity once site isolation is enforced.

Finally, we should note that the present kinetic model includes several simplifying assumptions; thus, its application for specific conditions may be limited. Only the coordination-insertion pathway of the Cossee-Arlman mechanism is considered, excluding alternative routes such as C_4H_8–C_4H_8 coupling or chain-transfer processes that may become relevant under particular reaction conditions. For example, in the study by Li et al.[22], the observed product distribution was dominated by C_4H_8 (39–46%) and C_8H_{16} (46–59%), with only 2–8% of C_6H_{12}, a pattern that may reflect additional pathways such as C_4H_8–C_4H_8 coupling that are not included in our current model. Mass transfer is represented by an effective diffusion length corresponding to an average diffusion path, without accounting for a distribution of path lengths or time-dependent changes such as pore blockage. In *flow* mode, a constant ethylene concentration is assumed, implying a feed rate much larger than the conversion rate. Consequently, the model is best interpreted as capturing mechanistic trends rather than making quantitative predictions for a specific experimental condition.

We also note that our model does not include any co-catalyst, whereas many experimentally studied Ni-MOF systems, operated with co-catalysts (e.g., Et_2AlCl, methylaluminoxane), were reported to exhibit high C_4H_8 selectivity at significantly lower temperatures and moderate pressures. As summarized by Rajapaksha et al.[19], numerous Ni-MOF/co-catalyst combinations operate effectively near 20–35 °C and 10–30 bar, consistently favoring dimerization over higher oligomer formation. In our case, in the *flow* mode, the selectivity of C_4H_8 should increase at 350 K, while in the *batch* mode, at 380–450 K.

In summary, our results demonstrate that the selectivity of Ni-based active centers in NU-1000 is not governed solely by electronic properties, but also by MOF framework topology, effective diffusion length, site density, mass transport, and reactor mode. The multiscale kinetic model developed here, therefore, enables predictive tuning of olefin distributions as a function of operating conditions and provides further guidelines for the catalyst design. Small effective diffusion length, moderate site densities, and reactor configurations that ensure rapid product removal, favor the formation of short olefins and mitigate catalyst deactivation. Extending this integrated approach to other porous framework materials and catalytic reaction types promises to accelerate the discovery of high-performance porous-supported catalysts with atom-level precision.

Methods

Energy barriers and elementary reaction rates

The periodic DFT protocol followed ref. 14. Electronic energies were corrected to TPSSh-D3(BJ) using the hierarchical cluster approach, $E^{\mathrm{TPSSh}} = E^{\mathrm{PBE-D3(BJ)}}_{\mathrm{PBC}} + (E^{\mathrm{TPSSh-D3(BJ)}}_{\mathrm{cluster}} - E^{\mathrm{PBE-D3(BJ)}}_{\mathrm{cluster}})$, where H-saturated cluster models were cut from the periodic framework, optimized at PBE-

D3(BJ)/def2-TZVP, and evaluated by single-point calculations at PBE-D3(BJ) and TPSSh-D3(BJ)/def2-QZVPP in ORCA 5.0.4. Thermal contributions for framework-bound intermediates and transition states were obtained from partial Hessians computed by finite differences (0.01 Å) within the harmonic approximation (two shallow imaginary modes were treated as one-dimensional free rotations), while gas-phase species were treated using the ideal-gas rigid-rotor harmonic-oscillator approximation, including the pressure correction $k_B T ln(p/p^\circ)$ with $p^\circ = 1$ atm. Activation free energies were defined as $\Delta G^{\ddagger}(T, p) = G_{TS}(T, p) - G_{reactant}(T, p)$, and elementary rate constants were computed using Eyring transition-state theory, $k(T, p) = (k_B T/h) \exp[-\Delta G^{\ddagger}(T, p)/(RT)]$.

Grand-canonical Monte Carlo simulations

GCMC simulations were fully performed following the protocol of our previous work[7]. In brief, all calculations were performed using RASPA 2.0.45[42] under a rigid-framework approximation, employing UFF4MOF parameters for the NU-1000 host and TraPPE + CHARMM36 parameters for the guest olefins. A $1 \times 1 \times 2$ supercell of NU-1000 was used together with a 12.5 Å Lennard–Jones cutoff. Production runs consisted of up to 10^7 Monte Carlo cycles of insertion–deletion moves for temperatures between 300 and 600 K and pressures between 1 and 50 bar. Compared to our previous study, the state-point grid is expanded and now includes 21 temperature points and 11 pressure points, providing a denser and more uniform (T, p) sampling for equimolar C_2H_4–$C_{10}H_{20}$ mixtures.

Adsorption is described using two complementary models that serve distinct roles within the multiscale framework. For single-component C_2H_4 adsorption, isotherms at each temperature were fitted to a single-site Langmuir model $n = n_{max}(T)\, b(T) f / [1 + b(T) f]$, where the fugacity $f = \phi(T, P)P$ was obtained from the Peng–Robinson equation of state. The temperature dependence of $n_{max}(T)$ and $b(T)$ was represented by polynomial fits, enabling smooth interpolation across the simulated temperature range for initializing the ethylene loading and boundary concentration (see Fig. S5). Competitive multicomponent adsorption of olefins under reaction conditions is captured using a k-nearest-neighbor (kNN) surrogate model trained on multicomponent GCMC data (see Fig. S3). This kNN model explicitly accounts for co-adsorption and competitive displacement among olefins of different chain lengths and provides composition-dependent in-pore loadings during the kinetic simulations. For olefin sizes $n > 10$, loadings were extrapolated assuming linearity in $ln(q)$ versus n over the C_6H_{12}–$C_{10}H_{20}$ range (see Fig. S4). Excess co-adsorption was calculated in RASPA as: $n_{exc} = n_{abs} - V_{pore}\, \rho_{bulk}$, where n_{abs} is the absolute uptake from GCMC, V_{pore} is the pore volume (from helium-void-fraction analysis), and ρ_{bulk} is the gas density at the same T and p. This excess uptake, which represents the net uptake by the MOF relative to an equal volume of bulk gas, was used to determine the capacity difference between the external reservoir and the MOF framework. The external reservoir capacity, defined as $\rho_{bulk} V_{pore}$, was also estimated using the same grouped kNN surrogate trained on GCMC bulk-phase density data to ensure a consistent T-p interpolation. For olefins with $n > 10$, where $\rho_{bulk} V_{pore}$ plateaus in the reference dataset, the surrogate holds this term fixed at the $C_{10}H_{20}$ value, reflecting the negligible chain-length dependence observed in our simulations.

Mass-transport

Self-diffusion coefficients of α-olefins in NU-1000 were estimated under infinite dilution by combining TST with Widom test-particle insertions as implemented in RASPA 2.0.45. Activation Gibbs free energies $\Delta G^{\ddagger}$ between adjacent adsorption sites were obtained via Widom insertions by measuring the reversible work for a test-particle to move along the minimum-energy path connecting neighboring sites. Diffusion coefficients were then computed as:

$$D_{TST} = \frac{\nu \lambda^2}{2d} \exp\left(-\Delta G^{\ddagger}/(k_B T)\right), \tag{2}$$

where λ is the site-to-site hopping distance that is, the spatial separation between two adjacent adsorption minima that an olefin must traverse during a single diffusion step, $d = 3$ is the dimensionality, and the thermal velocity prefactor associated with the diffusive hopping of adsorbates between adjacent sites was approximated by Eq. (3).

$$\nu = \sqrt{\frac{k_B T}{2\pi m}}, \tag{3}$$

with m as the molecular mass of each olefin. This procedure yielded D_0 values consistent with the infinite-dilution limit and provided the kinetic input for the master-equation solver. Energy profiles are provided in SI Fig. S2. Widom free-energy profiles were obtained from three independent simulations for each chain length, temperature, and crystallographic direction. Profiles were combined by inverse-variance weighting using block-averaged uncertainties, and the combined curves were smoothed using Gaussian Process Regression to obtain differentiable free-energy landscapes from which $\Delta G^{\ddagger}$ and hop distances λ were extracted for the TST model. Uncertainties are provided in SI Fig. S1.

Within transition-state theory (TST), the self-diffusion coefficient can be written as $D_{TST} \propto \nu \exp[-\Delta G^{\ddagger}/(k_B T)]$, where the attempt frequency obeys the physical scaling $\nu \propto \sqrt{T/m}$. To separate this trivial temperature dependence from the barrier-controlled kinetics, we defined a normalized diffusion quantity

$$y_n(T) = \frac{D_{TST}(n, T)}{\sqrt{T}}, \tag{4}$$

which removes the leading $(\sqrt{T})$ prefactor and yields a smoother, approximately linear dependence on temperature. Temperature was then standardized, $T_s = (T - \mu_T)/\sigma_T$, and for each olefin size $n \le 10$, an independent linear model

$$y_n(T_s) = a_n T_s + b_n \tag{5}$$

was fitted. Predictions were converted back to raw diffusion coefficients via $D_{pred} = y_n(T_s)\sqrt{T}$.

For longer olefins ($n > 10$), where explicit TST calculations were not available, we performed a mass-based extrapolation. At each query $n > 10$, we first evaluated the trained models for $n = 8$ and $n = 10$, obtaining $D_8(T)$ and $D_{10}(T)$. Each value was then scaled by the physically motivated factor $\sqrt{\frac{m_n}{m_{base}}}$ with m_n the molecular mass of olefin size n, to account for the $\nu \propto \sqrt{T/m}$ dependence. The final extrapolated diffusion coefficient was taken as the average of these scaled predictions. This procedure preserves (i) the thermal trends learned from the explicit TST calculations, (ii) the correct mass dependence of the attempt frequency, and (iii) smooth continuity across the full range of olefin sizes used in the kinetic simulations.

Multiscale kinetic model

Chemical transformations and inter-pore mass transport were treated in a unified set of ordinary differential equations (ODEs) based on master equation formalism:

$$\frac{dC_i}{dt} = \sum_j \nu_{ij} r_j \, (i = 1, \ldots, N_{sp}), \tag{6}$$

where C_i is the concentration of species i, ν_{ij} the stoichiometric coefficient in elementary step j, and r_j a mass-action rate.

Exchange between the gas-phase reservoir (g) and the MOF (m) is treated using a linear driving force (LDF) approximation expressed in terms of fractional filling $f^A = C^A/q^A$. The directional exchange rates are evaluated

separately as:

$$J^A_{g\to m} = k^A_d f^A_g = k^A_d \frac{C^A_g}{q^A_g},\ J^A_{m\to g} = k^A_d f^A_m = k^A_d \frac{C^A_m}{q^A_m}, \tag{7}$$

and the net exchange term entering the MOF balance is

$$J^A = J^A_{g\to m} - J^A_{m\to g} = k^A_d \left(\frac{C^A_g}{q^A_g} - \frac{C^A_m}{q^A_m}\right). \tag{8}$$

At dynamic equilibrium, $J^A_{g\to m} = J^A_{m\to g}$ and thus $J^A = 0$. Here, q^A_m is the MOF adsorption capacity (saturation loading) of species A obtained from the GCMC-based adsorption surrogates, while q^A_g is a gas-phase reference concentration computed from an equation of state and used to normalize C^A_g. The LDF rate constant is:

$$k^A_d = \frac{15\, D_A}{R^2}, \tag{9}$$

with D_A as the (self-)diffusion coefficient of A in the MOF and $2 \times R = L$ as the effective diffusion length.

The solver was packaged as a lightweight Python module (`kinetic_model.core.reactor`) that transforms a human-readable reaction list into the full ODE system. Each step is supplied as:

[`reaction_str`, $k_f(k_r)$],

where `reaction_str` may be `"A + B -> C"` (irreversible), `"A + B <-> C + D"` (reversible), or `"X@A <D> X@B"` (diffusive exchange, with `@` denoting the compartment). Optional keyword arguments accept (i) a dictionary of adsorption capacities for each compartment, (ii) a list of buffered species (`fixed_concentrations`), (iii) initial concentrations, and (iv) a NumPy time grid. A single call:

`solve(initial_concs, time_grid)`

integrates the automatically generated ODEs with LSODA at relative/absolute tolerances $10^{-9}/10^{-12}$ and returns the result as a `pandas.DataFrame`.

Reactor-operation modes

Two limiting reactor configurations were simulated. In both cases, the resulting ODE system was integrated with the master-equation solver described above, allowing direct comparison of *infinite crystal*, *batch*, and *flow* modes.

In *batch* (closed-cell) mode, the reactor was initialized with ethylene at its equilibrium gas-phase concentration for the chosen T–p point, all higher olefins being zero. Mass exchange between the NU-1000 framework and the external reservoir was permitted for every species and was described by the pseudo-first-order flux.

In *flow* (continuous-removal) mode, ethylene was held at its inlet concentration throughout ($dC_{C_2H_4}/dt = 0$), representing a constant feed. For all products, the diffusive term was mono-directional MOF → reservoir, enforcing their immediate elution and precluding re-adsorption. This mimicked a *flow* reactor mode in which fresh gas sweeps products away while sustaining the ethylene partial pressure.

We additionally performed a Boltzmann simulation for thermodynamic equilibrium state calculation, which corresponded to the *infinite-crystal* scenario where detailed balance holds, and all reactions are fully reversible. The distribution of species was calculated according to the Boltzmann law:

$$p_i = \frac{\exp(-\beta G_i)}{Z}, \tag{10}$$

where G_i is the Gibbs free energy of species i, $\beta = 1/(k_B T)$, and $Z = \sum_i \exp(-\beta G_i)$ is the partition function ensuring normalization. This approach represents the thermodynamic steady state, in which the system composition is determined purely by equilibrium energetics without kinetic or diffusional limitations.

Data availability

The data supporting the findings of this study are available in the NOMAD repository under https://doi.org/10.17172/NOMAD/2026.02.12-3. The dataset contains the simulation outputs generated with the code version archived at the time of data production.

Code availability

The most up-to-date development version of the kinetic modeling framework is publicly available at https://github.com/multiscale-modelling/kinetic_model.git.

Received: 23 December 2025; Accepted: 9 March 2026;
Published online: 24 March 2026

References

1. Ess, D., Gagliardi, L. & Hammes-Schiffer, S. Introduction: computational design of catalysts from molecules to materials. *Chem. Rev.* **119**, 6507–6508 (2019).
2. Sauer, J. The future of computational catalysis. *J. Catal.* **433**, 115482 (2024).
3. Bordonhos, M. et al. Multiscale computational approaches toward the understanding of materials. *Adv. Theory Simul* **6**, 2200628 (2022).
4. Wehinger, G. D. et al. Quo vadis multiscale modeling in reaction engineering? - a perspective. *Chem. Eng. Res. Des.* **184**, 39–58 (2022).
5. Bernales, V. et al. Computationally guided discovery of a catalytic cobalt-decorated metal–organic framework for ethylene dimerization. *J. Phys. Chem. C. Nanomater. Interfaces* **120**, 23576–23583 (2016).
6. Ye, J., Gagliardi, L., Cramer, C. J. & Truhlar, D. G. Single ni atoms and ni4 clusters have similar catalytic activity for ethylene dimerization. *J. Catal.* **354**, 278–286 (2017).
7. Avdoshin, A., Wenzel, W. & Kozlowska, M.Confinement-modulated diffusion of alkenes in nu-1000 framework material. *Chem. Commun.* https://doi.org/10.1039/D5CC01329A (2025).
8. Hulea, V. Nickel-aluminosilicate catalysts for ethylene oligomerization: recent scientific progress. *Catal. Sci. Technol.* **15**, 4612–4631 (2025).
9. Li, L., Xu, X., Ye, M. & Liu, Z. Toward realistic simulations of zeolite catalytic processes: a mini review. *J. Phys. Chem. C.* **129**, 24–36 (2024).
10. Zheng, J. et al. Metal-organic framework supported single-site nickel catalysts for butene dimerization. *J. Catal.* **413**, 176–183 (2022).
11. Löbbert, L. et al. Influence of 1-butene adsorption on the dimerization activity of single metal cations on UiO-66 nodes. *J. Am. Chem. Soc.* **145**, 1407–1422 (2023).
12. Le, T.-H. T., Ferro-Costas, D., Fernández-Ramos, A. & Ortuño, M. A. Combined DFT and kinetic Monte Carlo study of UiO-66 catalysts for γ-valerolactone production. *J. Phys. Chem. C. Nanomater. Interfaces* **128**, 1049–1057 (2024).
13. Dohrmann, N., King, D. S., Gaggioli, C. A. & Gagliardi, L. Challenge of small energy differences in metal–organic framework reactivity. *J. Phys. Chem. C. Nanomater. Interfaces* **127**, 16891–16900 (2023).
14. Huynh, T.-N., Matsokin, N. A., Studt, F., Fink, K. & Sharapa, D. I. Ethylene dimerization on Ni-supported Nu-1000: a comprehensive theoretical study. *J. Phys. Chem. C* **129**, 51 (2025).
15. Smit, B. & Maesen, T. L. M. Molecular simulations of zeolites: adsorption, diffusion, and shape selectivity. *Chem. Rev.* **108**, 4125–4184 (2008).
16. Haag, W. Catalysis by zeolites – science and technology. *Stud. Surf. Sci. Catal*. 1375–1394 https://www.sciencedirect.com/science/article/pii/S0167299108636800 (1994).
17. Bickel, E. E. & Gounder, R. Hydrocarbon products occluded within zeolite micropores impose transport barriers that regulate brønsted acid-catalyzed propene oligomerization. *JACS Au* **2**, 2585–2595 (2022).
18. Finiels, A., Fajula, F. & Hulea, V. Nickel-based solid catalysts for ethylene oligomerization – a review. *Catal. Sci. Technol.* **4**, 2412–2426 (2014).

19. Rajapaksha, R., Samanta, P., Quadrelli, E. A. & Canivet, J. Heterogenization of molecular catalysts within porous solids: the case of Ni-catalyzed ethylene oligomerization from zeolites to metal–organic frameworks. *Chem. Soc. Rev.* **52**, 8059–8076 (2023).
20. Mondloch, J. E. et al. Vapor-phase metalation by atomic layer deposition in a metal–organic framework. *J. Am. Chem. Soc.* **135**, 10294–10297 (2013).
21. Goetjen, T. A., Zhang, X., Liu, J., Hupp, J. T. & Farha, O. K. Metal–organic framework supported single site chromium(iii) catalyst for ethylene oligomerization at low pressure and temperature. *ACS Sustain. Chem. Eng.* **7**, 2553–2557 (2019).
22. Li, Z. et al. Sintering-resistant single-site nickel catalyst supported by metal–organic framework. *J. Am. Chem. Soc.* **138**, 1977–1982 (2016).
23. Platero-Prats, A. E. et al. Bridging zirconia nodes within a metal–organic framework via catalytic Ni-hydroxo clusters to form heterobimetallic nanowires. *J. Am. Chem. Soc.* **139**, 10410–10418 (2017).
24. Ye, J., Gagliardi, L., Cramer, C. J. & Truhlar, D. G. Computational screening of mof-supported transition metal catalysts for activity and selectivity in ethylene dimerization. *J. Catal.* **360**, 160–167 (2018).
25. Liu, Y. M. & Smit, B. Predicting product distribution of propene dimerization in nanoporous materials. *ACS Catal.* **7**, 3940–3948 (2017).
26. Johnson, M. S. et al. Rmg database for chemical property prediction. *J. Chem. Inf. Model.* **62**, 4906–4915 (2022).
27. Liu, M. et al. Reaction mechanism generator v3.0: advances in automatic mechanism generation. *J. Chem. Inf. Model.* **61**, 2686–2696 (2021).
28. Glowacki, D. R., Liang, C.-H., Morley, C., Pilling, M. J. & Robertson, S. H. Mesmer: an open-source master equation solver for multi-energy well reactions. *J. Phys. Chem. A* **116**, 9545–9560 (2012).
29. Zádor, J. et al. Automated reaction kinetics of gas-phase organic species over multiwell potential energy surfaces. *J. Phys. Chem. A* **127**, 565–588 (2023).
30. Shannon, R. J., Martínez-Nùñez, E., Shalashilin, D. V. & Glowacki, D. R. Chemdyme: Kinetically steered, automated mechanism generation through combined molecular dynamics and master equation calculations. *J. Chem. Theory Comput.* **17**, 4901–4912 (2021).
31. Webber, T. E. et al. Size control of the mof nu-1000 through manipulation of the modulator/linker competition. *Cryst. Growth Des.* **20**, 2965–2972 (2020).
32. Yeh, B. et al. Structure and site evolution of framework ni species in mil-127 mofs for propylene oligomerization catalysis. *J. Am. Chem. Soc.* **145**, 3408–3418 (2023).
33. Yeh, B. et al. Validation of the cossee–arlman mechanism for propylene oligomerization on ni/uio-66. *Catal. Sci. Technol.* **13**, 4213–4222 (2023).
34. Vargas, E. L. & Snurr, R. Q. Heterogeneous diffusion of alkanes in the hierarchical metal–organic framework nu-1000. *Langmuir* **31**, 10056–10065 (2015).
35. Song, L. et al. Mof-supported diimine nickel catalyst for highly active and selective ethylene dimerization. *ACS Catal.* **15**, 12590–12597 (2025).
36. Chen, C. et al. Ultra-highly active ni-doped mof-5 heterogeneous catalysts for ethylene dimerization. *Small* **19**, 2301235 (2023).
37. Guo, W., Wang, Z., Wang, X. & Wu, Y. General design concept for single-atom catalysts toward heterogeneous catalysis. *Adv. Mater.* **33**, 2004287 (2021).
38. Zhao, L. et al. Coordination anchoring synthesis of high-density single-metal-atom sites for electrocatalysis. *Coord. Chem. Rev.* **466**, 214603 (2022).
39. Hou, C.-C., Wang, H.-F., Li, C. & Xu, Q. From metal–organic frameworks to single/dual-atom and cluster metal catalysts for energy applications. *Energy Environ. Sci.* **13**, 1658–1693 (2020).
40. Yeh, B. et al. Site densities, rates, and mechanism of stable ni/uio-66 ethylene oligomerization catalysts. *J. Am. Chem. Soc.* **143**, 20274–20280 (2021).
41. Liu, J. et al. Beyond the active site: tuning the activity and selectivity of a metal–organic framework-supported Ni catalyst for ethylene dimerization. *J. Am. Chem. Soc.* **140**, 11174–11178 (2018).
42. Dubbeldam, D., Calero, S., Ellis, D. E. & Snurr, R. Q. Raspa: molecular simulation software for adsorption and diffusion in flexible nanoporous materials. *Mol. Simul.* **42**, 81–101 (2015).

Acknowledgements

This research was funded by the Deutsche Forschungsgemeinschaft (DFG) via GRK 2450. The authors gratefully acknowledge support of the state of Baden-Württemberg via access to the bwHPC (bwUnicluster), the German Research Foundation (DFG) through grant no. INST 40/575-1 FUGG (JUSTUS 2 cluster, RVs bw17D011 and bw15C003) and the computing time provided on the high-performance computer HoreKa by the National High-Performance Computing Center at KIT (NHR@KIT), funded by the Ministry of Science, Research and the Arts Baden-Württemberg, the Federal Ministry of Education and Research, and partly by DFG. We acknowledge support by the KIT-Publication Fund of the Karlsruhe Institute of Technology.

Author contributions

A.A. developed the methodology, software development, implemented the computational framework, performed the simulations and formal analysis, curated the data, and wrote the original draft. N.A.M. contributed to methodology, validation, formal analysis, data curation, and visualization. T.-N.H. contributed to methodology development, software development, validation, formal analysis, and data curation, and participated in writing and visualization. D.I.S., K.F., F.S., W.W., and M.K. conceived the project, supervised the research, and acquired funding. All authors reviewed and edited the manuscript and approved the final version.

Funding

Open Access funding enabled and organized by Projekt DEAL.

Competing interests

The authors declare no competing interests.

Additional information

Supplementary information The online version contains supplementary material available at https://doi.org/10.1038/s41524-026-02044-7.

Correspondence and requests for materials should be addressed to Mariana Kozlowska.